electronics

MDPI

Article

Optimization of Multi-Phase Motor Drive System Design through Thermal Analysis and Experimental Validation of Heat Dissipation

Jun-Shin Park [1,†], Tae-Woo Lee [1,2,†], Jae-Woon Lee [2], Byoung-Gun Park [1,2] and Ji-Won Kim [1,2,*]

[1] Department of Energy and Power Conversion Engineering, Korea University of Science and Technology, Daejeon 34113, Republic of Korea; jsp@keri.re.kr (J.-S.P.); twlee@keri.re.kr (T.-W.L.); bgpark@keri.re.kr (B.-G.P.)
[2] Electric Machine and Drive Research Center, Korea Electrotechnology Research Institute, Changwon 51543, Republic of Korea; lucky_ox@keri.re.kr
* Correspondence: jwkim@keri.re.kr; Tel.: +82-55-280-1402
† These authors contributed equally to this work.

Abstract: In power semiconductor systems such as inverters, managing losses is critical for optimizing performance. Inverters, which convert DC to AC for applications such as renewable energy systems, motor drives, and power supplies, are significantly affected by the thermal performance of components such as metal-oxide-semiconductor field-effect transistors (MOSFETs). Efficient thermal management is critical for the longevity and performance of power electronic systems, especially in high-power applications. Designing effective thermal management strategies for inverters reduces losses, increases efficiency, and improves performance while considering space constraints and complex component interactions. In this study, power electronics simulations and computational fluid dynamics (CFD) thermal analysis were integrated to design the inverter. Using an integrated simulation, a thermal analysis was performed based on the inverter losses per module. A power electronics simulation was used to verify the validity of the loss values in the inverter design, and the CFD thermal analysis facilitated the visual analysis of the variables to be considered. The validity of the design was evaluated through experimental verification of the inverter system. A temperature saturation of 63.9 °C at 60A_{rms} was recorded in the simulation, and a temperature saturation of 45 °C or less at 59A_{rms} to 60A_{rms} was obtained for each phase in the actual test. Considering the ambient temperature difference, it showed a difference of approximately 9.9 °C. This conclusion allows us to reduce the high probability of risk derived by considering a small margin of safety for each variable in the design. This solution can be used to compactly design real inverters and solve complex thermal problems in power semiconductor-based systems. Finally, this study analyzes the similarities and differences between CFD simulations, power electronics simulations, and real-world experimental validation, highlighting the importance of thermal management in improving the efficiency of power electronic systems, particularly inverters.

Keywords: electric propulsion systems; motor drive; inverter; CFD (computational fluid dynamics); IMS (insulated metal substrate); MOSFET (metal-oxide-semiconductor field-effect transistor); heat dissipation; switching losses; conduction losses

check for updates

Citation: Park, J.-S.; Lee, T.-W.; Lee, J.-W.; Park, B.-G.; Kim, J.-W. Optimization of Multi-Phase Motor Drive System Design through Thermal Analysis and Experimental Validation of Heat Dissipation. *Electronics* **2023**, *12*, 4177. https://doi.org/10.3390/electronics12194177

Academic Editor: Kan Akatsu

Received: 4 September 2023
Revised: 26 September 2023
Accepted: 7 October 2023
Published: 9 October 2023

Copyright: © 2023 by the authors. Licensee MDPI, Basel, Switzerland. This article is an open access article distributed under the terms and conditions of the Creative Commons Attribution (CC BY) license (https://creativecommons.org/licenses/by/4.0/).

1. Introduction

With the growing global concern for environmental issues, the propulsion of mobility with various fossil fuel propulsion systems is changing. This change in propulsion is characterized by a shift from fossil fuel-based propulsion to electric propulsion. The main reason for this shift is the negative impact of carbon and nitrogen compounds from fossil fuel-consuming propulsion systems [1]. As regulations on compounds are tightening internationally, research on reducing emissions from propulsion systems, such as carbon capture utilization and storage (CCUS) [2,3], is already underway, and at the same time,

fossil fuel propulsion systems are changing to electric propulsion. The market for electric propulsion is growing, and changes in the way mobility is propelled are inevitable [4,5]. As the mobility industry is already shifting to electric propulsion, electric motors and inverters, which are the core of electric propulsion systems, are very important. However, there are many variables in the characteristics of propulsion mobility and the driving environment; therefore, there are many differences in the form and control methods of electric motors and inverters in different fields of mobility. In the case of automotive mobility, battery electric vehicle (BEV)/hybrid electric vehicle (HEV) mobility, where many companies are already using three-phase voltage-source inverters and corresponding electric motors, are the most dominant [6]. In the field of marine mobility with electric ships and outboard thrusters or in the field of aviation mobility with personal air vehicles (PAVs), there can be many harsh environments for electric motors. Stable operation is important, but it is also important to prepare the compensation system for failures; therefore, fault tolerance is often considered [7,8]. Multi-phase motors may be appropriate when operating in environments that need to be fault-tolerant, and in the electric vehicle (EV) business, they can be operated regardless of mobility. Multi-phase electric motor drive systems have many advantages over traditional three-phase drive systems, including a higher allowable current per phase, higher allowable voltage per phase, and improved magneto motive force (MMF) [9].

However, multi-phase motors come in many forms, ranging from N-phase motors with numerous phases to motors that require variable six-phase and dual three-phase operation. In the case of dual three-phase motors, the number of inverter legs can be configured to six; however, depending on the topology, the structure of the inverter becomes complicated [10]. Therefore, it is not easy to cope with a single three-phase voltage-source inverter, and there may be a disadvantage in that a new inverter must be designed according to the shape. If the output of the inverter is set too high for stable operation and then designed and manufactured according to the shape of the motor, it can be easily designed; however, it cannot be efficiently designed, and the budget cannot be reduced in the inverter's design and manufacturing stage. Therefore, it is important to design it according to the output capacity at the design stage, which is related to the inverter loss analysis.

Because the losses in an inverter are in the form of heat, even with good control performance techniques, if the heat of the device is not dissipated quickly, it is bound to cause thermal runaway of the power semiconductor, which in turn leads to burnout of the power semiconductor device, which greatly affects both the efficiency and stable operation of the entire system. Therefore, it is important to analyze the heat source in the inverter design stage, and simulation verification is often performed using thermal analysis simulation, regardless of the mobility field [11–14].

In this study, an inverter for use with multi-phase motors was designed and experimentally validated, and improvements to that work include the following:

- The design attempted to overcome the limitations with significant modularity to accommodate not only six-phase and dual three-phase but also various multi-phase motors in the future.
- To make it easier to expand the capacity of each unit inverter, thermal analysis was performed in the form of a unit and an overall configuration to prevent thermal runaway of individual unit inverters, and various variables were considered in the verification stage.
- By comparing the simulation results with the actual experimental verification, the completeness of the simulation was verified in the design for modular inverters for multi-phase motors.

2. Inverter Design and Structure for Multi-Phase Motor Drive System

When designing a multi-phase inverter compared with a traditional three-phase inverter, each equivalent current requirement decreases as the number of phases increases [6] for an inverter with the same output capacity. This study does not compare three-phase and N-phase motors of the same output but designs an inverter that has the advantage

of flexible capacity expansion through a substantial modular inverter configuration when driving various multi-phase motors. The two motors used were outboard motors for electric propulsion ships, with outputs of 3 kW and a multi-phase of 10 kW. The inverter module was a two-level inverter and was designed using metal-oxide-semiconductor field-effect transistors (MOSFETs). The design was based on a DC 48 V three-phase output and was set to a fairly high continuous current of $80A_{rms}$. To achieve a design close to the ideal value, the inverter phase current needed to be designed at $60A_{rms}$, but considering variables such as motor efficiency, power factor, and tolerance, the value was set as a constant current value. The peak values of the current were multiplied by approximately 1.2, the power P was 3 kW, the motor efficiency K_{eff} was set to approximately 0.92, and the power factor PF was set to 0.9. The capitalized M is the inverter phase current margin. The designed phase current value of I_{PHRMS} is as follows:

$$I_{PHRMS} = \frac{P}{\frac{V_{DC} \times 3 \times K_{eff} \times PF}{\sqrt{2} \times \sqrt{3}}} \times 1.2 + M \tag{1}$$

Once the basic power of the inverter had been set and the current to be designed had been set, it was necessary to consider reducing this loss. Inverter loss is inevitably always present and is released in the form of heat, which is an important cause of inverter performance degradation and failure. Therefore, reducing inverter loss leads to an inverter heat dissipation design, which can contribute significantly to reducing the failure of power semiconductor devices. To improve the loss reduction for an inverter's thermal design, the first step is to analyze the inverter's heat source losses. There are many types of inverter losses, including conduction loss, switching loss, dead-time loss, gate charge loss, and integrated circuits (ICs). Among these losses, conduction and switching losses are the largest variables in inverter thermal design [15–17]. The other losses are not as significant as the conduction and switching losses. Compared with the conduction and switching losses, they were excluded and not reflected in the simulation. The inverter we considered was one that used parallel MOSFETs. Parallel MOSFETs in inverters have obvious advantages in reducing conduction losses and balancing currents [18]. There is a trade-off between the number of parallel elements and the overall size of the inverter; the larger the number of parallel elements, the larger the overall inverter size. Therefore, to consider the above, we applied it to the design based on the graph in (3), which shows the relationship between the number of parallel MOSFETs and the loss through the equation in (2). $P_{C/FET}$ is the conduction loss value per MOSFET, $P_{SW/FET}$ is the switching loss value per MOSFET, and I_{PH} is the RMS value of the phase current. R_{DS} is the on resistance of the MOSFET. n is the number of parallel connections of the MOSFETs, V_{DC} is the DC voltage, t_{on} is the sum of the rise time of the V_{ds} of the MOSFET and the fall time of the MOSFET drain current I_d, t_{off} is the sum of the fall time of the MOSFET's V_{ds} and the rise time of the MOSFET's drain current I_d, and f_{sw} is the inverter's switching frequency.

$$P_{C/FET} \approx \frac{\left(\frac{I_{PH}}{\sqrt{2}}\right)^2 \times R_{DS}}{n^2} \tag{2}$$

$$P_{SW/FET} \approx \frac{\left(0.5 \times 0.5 \times V_{DC} \times I_{PH} \times f_{sw} \times \left(t_{on} + t_{off}\right)\right)}{n} \tag{3}$$

Figure 1 shows that the loss value decreases as the number of parallel connections of MOSFETs in the inverter varies When five MOSFETs were connected in parallel, the loss per FET was the smallest, and considering the overall inverter size and loss reduction, it was designed with five parallel connections, as shown in the figure below.

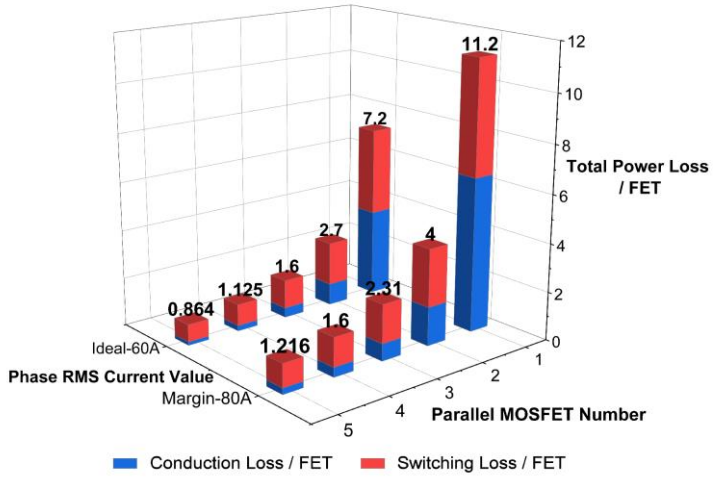

(**a**)

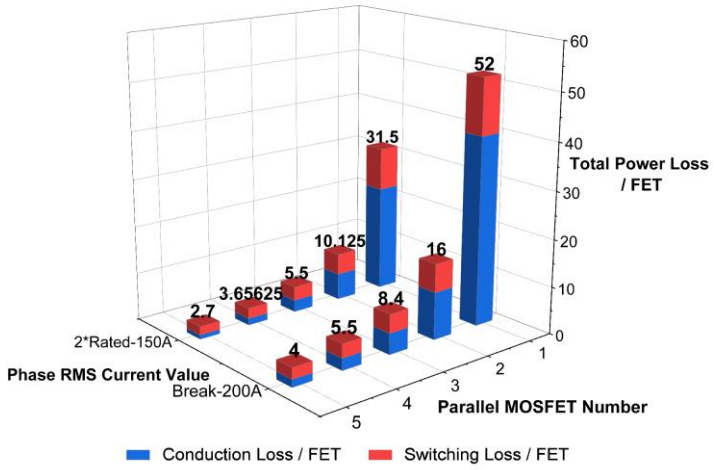

(**b**)

Figure 1. Loss graph as a function of the number of MOSFET parallel connections. And phase current values: (**a**) rated current value: $60A_{rms}$, designed current value: $80A_{rms}$; (**b**) two times the designed value: $150A_{rms}$, device breakdown current value: $200A_{rms}$.

The inverter was organized per unit module, making it suitable for parallelization. Because the total output capacity is determined by the number of inverter modules configured in parallel, heat loss analysis begins with the analysis of a single inverter module, which is the smallest unit. The structure and form of that inverter module can be seen in Figure 2.

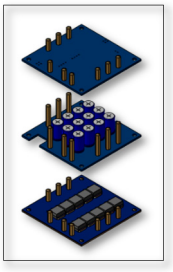

(**a**)

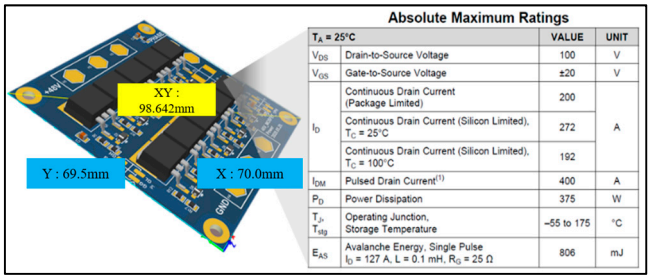

(**b**)

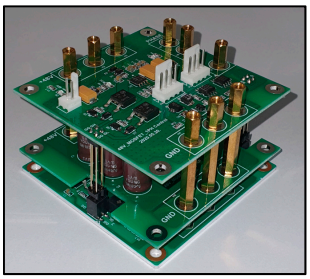

(**c**)

Figure 2. Modular unit inverter for multi-phase motor: (**a**) Layer-by-Layer model of a unit inverter; (**b**) Specification of the MOSFET part of the Inverter; (**c**) Image of the assembled inverter.

3. Simulations for Multi-Phase Inverter Design

Based on the inverter loss value, several simulations were performed for inverter design feasibility. For power electronics simulations, simulation is possible if the analytical and mathematical requirements of the inverter circuit are satisfied. However, for CFD analysis, the inverter structure must be identified in advance, and the physical properties and boundary conditions must be set. The inverter in question utilized an insulated metal substrate (IMS) structure on a printed circuit board (PCB) for fast heat transfer. As a major feature of IMS boards, aluminum is inserted inside the layer; therefore, information about its physical properties affects the simulation. As shown in Figure 3, the IMS board is composed of three materials, aluminum, copper, and FR-4, and the MOSFET is composed of aluminum, Epoxy Molding Compound (EMC), and iron.

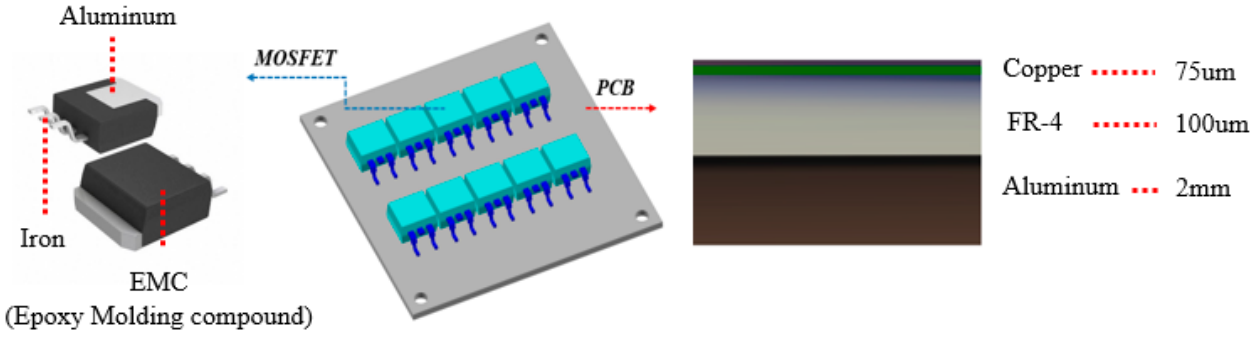

Figure 3. IMS board and MOSFET configuration properties for analysis.

The MOSFET used in the inverter to be simulated was a Si-MOSFET, which is a MOSFET package that can be mounted on a PCB. The MOSFET package consists of a lead frame, lead wires, die bonding between the chip and lead frame, and a MOSFET chip. The source and gate of the MOSFET are connected to the lead frame and lead wires through bond wires. The form of mounting on the PCB is often configured as shown in Figure 4, and the capacity of the rated drain current that can flow is different for each capacity of the MOSFET; therefore, the loss and heat generation are different for each product type and parameter. Except for the losses affected by the control techniques, the losses and heat generated by the current flow are due to conduction losses as the MOSFET's current passes through the drain–source path and is affected by the package resistor value R_{DS}(on) and the drain current magnitude.

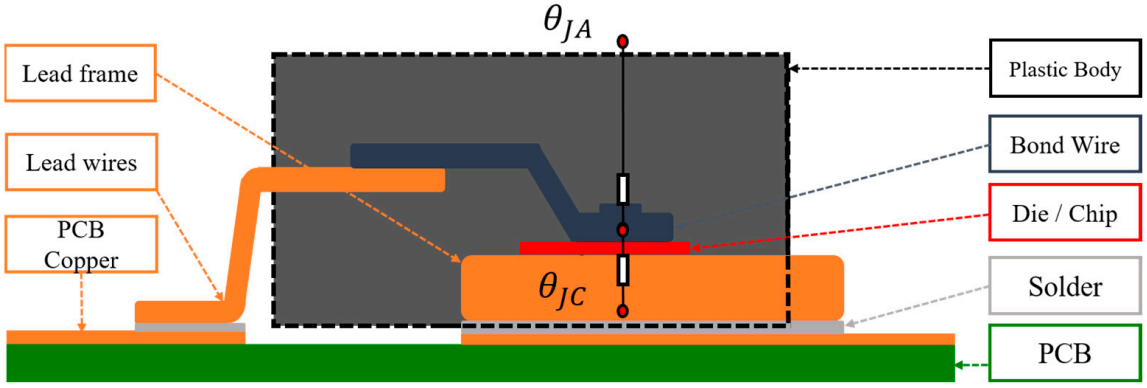

Figure 4. Cross-section of PCB-mounted D2PAK MOSFET package.

3.1. Power Analysis for Inverter Module and CFD Analysis

3.1.1. Power Electronics Analysis

To determine the suitability of the selected device for the inverter capacity and topology, loss values were calculated using the PowerForge® and PLECS® simulation

tools [19,20]. The MOSFET device was a CSD19536KTT device, and the analysis was based on its parameter values. Each leg of the inverter consisted of 10 MOSFETs. As shown in Table 1, the analysis was performed in a parallel connection configuration, with five MOSFETs at the bottom and top of each cell unit.

Table 1. Specifications of MOSFETs mounted in inverter.

Cell	Device	Package	Number of MOSFETs in	V_{rated}	I_{rated}
Cell 1 Bottom	Si MOSFET (CSD19536KTT)	TO-263	5 (Connected in Parallel)	100 V	272 A
Cell 1 Top			5 (Connected in Parallel)		
Cell 2 Bottom			5 (Connected in Parallel)		
Cell 2 Top			5 (Connected in Parallel)		
Cell 3 Bottom			5 (Connected in Parallel)		
Cell 3 Top			5 (Connected in Parallel)		

Simulations were performed to derive the loss value from the rated torque using the motor and inverter parameters listed in Tables 1 and 2. These simulations were based on the module-level design of the inverter; however, they were organized based on the three-phase configuration, which is the smallest unit that can be considered when driving an actual motor. Therefore, it was an analysis of a two-level three-phase inverter based on a 3 kW motor, and the analysis results were derived from the bottom and top parts that formed the legs of the designed inverter. The bottom and top of the legs consisted of the same MOSFET device parameters and parallel connection configuration. Therefore, each inverter module, that is, Cells 1, 2, and 3, which constitute a total of three phases, had the same loss value. The bottom leg loss values of Cell 1 are listed in Table 3. As each cell consisted of two legs, the value corresponding to twice the value was the loss that appears for each cell. Therefore, the P_C(W) per cell value corresponded to 4.434, and the P_{SW}(W) per cell value corresponded to 3.526, as in the form of the graph in Figure 5. In the simulation analysis, a three-phase inverter value of 23.886 W was found at approximately 1800 RPM and 16N·m and the loss values of speed and torque are shown in Figure 6. The inverter losses for this motor tended to increase or decrease consistently depending on the speed and torque of the motor.

Table 2. Parameter values of 3 kW motor and inverter for simulation.

Parameters	Symbols	Values
DC-link voltage	V_{DC}	48 V
Rated speed	RPM	1800 RPM
Rated torque	N·m	16 N·m
Number of poles	-	10
Switching frequency	Hz	10,000 Hz
Direct-axis inductance	H	76.5 µH
Quadrature-axis inductance	H	81.4 µH
Stator resistance	Ω	17.1 mΩ
Flux linkage	Wb	24.3 mWb

Table 3. Loss values on the bottom side of the 3-phase inverter in leg.

Cell	Conduction Type	$I_{rms}(A)$	$P_{cond}(W)$	$P_{SW,}OFF(W)$	$P_{SW,}ON(W)$	$P_{total}(W)$
Cell 1 Bottom						
	Forward	50.5	1.93	0.449	1.01	3.39
	Reverse	19.4	0.287	0.304	-	0.591
	Total	54.1	2.217	0.753	1.01	3.981

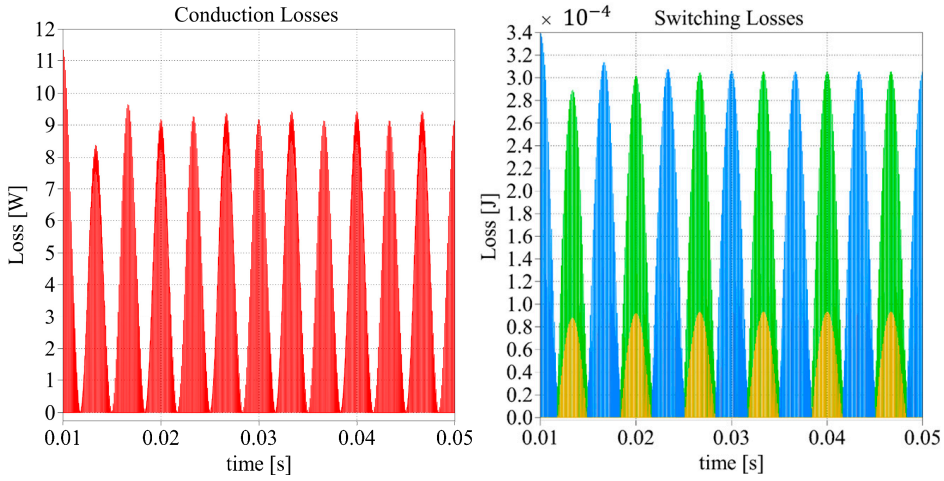

Figure 5. Conduction loss and switching loss.

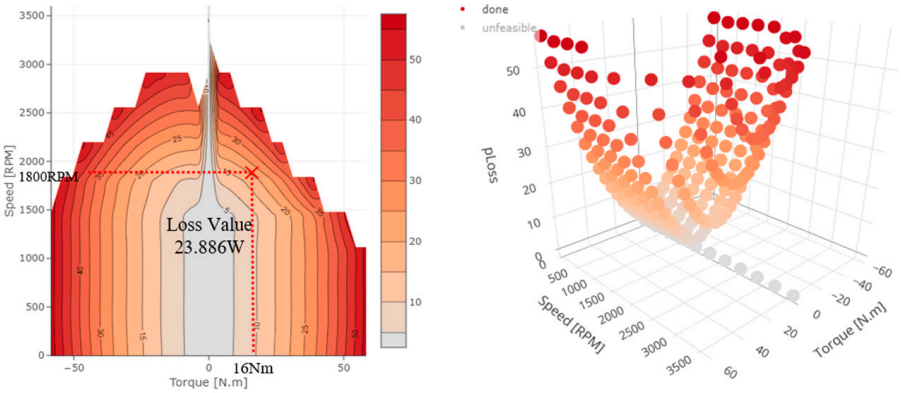

Figure 6. Plot of macro cell losses.

By conducting a pulse-width modulation (PWM) simulation with the three-harmonic injection method and the actual motor parameter values, the I_d current value was approximately 54.1A_{RMS}. This was similar to the rated current of 60A_{RMS} considered in the design phase, and when 54.1A_{RMS} was substituted into the loss formula used in the design phase, the total loss of the three-phase inverter was 22.98 W. This was about 0.9 W different from the 23.88 W found in the simulation analysis. The loss values assumed during the design process did not assume the diode parameters of the MOSFETs; therefore, the ratio of conduction losses to switching losses could be different because of the difference in considering the losses associated with the diodes.

3.1.2. CFD Analysis

After performing a power electronics analysis based on the loss, we performed CFD analysis. This analysis was modeled using the commercial CFD tools Altair® and Autodesk® [21,22]. The simulation conditions and parameters are listed in Tables 4 and 5, respectively. As shown in Figure 7, the domain wall of the boundary condition was approximately five times the volume of the horizontal length of the analysis object, and this condition was used to interpret the radiation. Although the guidelines of the domain wall differ depending on the target and type to be interpreted, we selected them by considering the trade-off between the reliability of the [23–25] interpretation and excessive simulation time. To facilitate the convergence of the analysis results, the domain wall was assumed to be convective rather than a constant-temperature setting analysis, and the corresponding heat transfer coefficient (HTC) value was set to 30 based on the HTC value of air [26]. The internal HTC value was set to 20, approximating the midpoint of the air HTC value,

to facilitate the comparison of internal effects according to the design variables. Table 5 lists the material parameters used in the analysis, which were based on the Autodesk® CFD database values, and the EMC material parameters were averaged from [27–29]. The process of temperature calculation can be simply expressed as a heat transfer equation, as shown in Equations (4) and (5) [30,31]. λ_x, λ_y, and λ_z represent the thermal conductivities in the x-, y-, and z-directions respectively. q_v is the sum of each heat source density. T is the temperature of the position in the solution region and T_f is the ambient temperature. S is the boundary surface and k is the heat transfer coefficient of $S_{1,2}$. α is the heat transfer coefficient of the solution boundary.

$$\frac{\partial}{\partial x}\left(\lambda_x \frac{\partial T}{\partial x}\right) + \frac{\partial}{\partial y}\left(\lambda_y \frac{\partial T}{\partial y}\right) + \frac{\partial}{\partial z}\left(\lambda_z \frac{\partial T}{\partial z}\right) = -q_v \tag{4}$$

$$k\frac{\partial T}{\partial n}|s_{1,2} = \alpha(T - T_f) \tag{5}$$

The most important part of the inverter that we focused on was the MOSFET element. The design value for the current margin was approximately $80A_{RMS}$, even if the device was subjected to severe conditions of $150A_{RMS}$, which was twice the rated value. However, even if a critical condition of $150A_{RMS}$, which was twice the rated value, was applied in anticipation of partial failure of the device, to determine whether normal inverter operation was possible with natural cooling or whether forced cooling should be adopted in consideration of the worst case, simulations were performed in advance.

Table 4. Conditions for CFD analysis.

Conditions	Condition Details	Values
Governing equations	Equations Energy equation Turbulence modeling	Navier–Stokes eq. Advective diffusive N/A (laminar)
Boundary conditions	Domain walls with radiation HTC (heat transfer coefficient) Temperature	-- 30 W/(m^2·°C) 27 °C (300 K)
Environmental conditions (air)	Density Dynamic viscosity Temperature	1.225 kg/m^3 1.781 × 10^{-5} Pa·s 27 °C (300 K)
Convection effect	HTC (heat transfer coefficient) Temperature	20 W/(m^2·°C) 27 °C (300 K)
Radiation effect	Emissivity	0.9
Y+ check	<20.0	1.5
Mesh type/number	Boundary layer mesh	1.2 M<
Heat density	Each per MOSFET	9.768 (W/mm^3)
Analysis type	Transient (time step)	1 s

Table 5. Material parameters and values.

Material	Density (kg/m^3)	Thermal Conductivity (W/m·°C)	Specific Heat (J/kg·°C)
Aluminum	2707	204	896
Copper	8934	380	380
EMC	1900 [27]	0.8 [28]	800 [29]
FR-4	1820	0.29	1150
Iron	7849	59	460

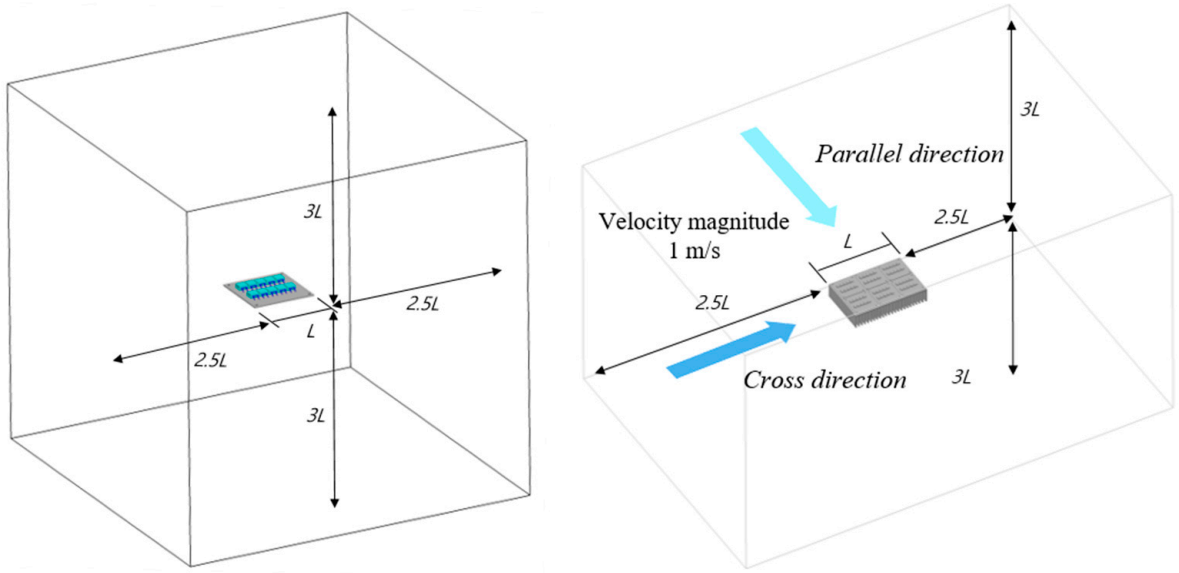

Figure 7. Domain wall and airflow settings for inverter CFD.

In Figure 8, the CFD analysis shows the temperature of the inverter as the current is applied under hard conditions. At twice the rated current, the temperature was 114.85 °C, and the MOSFET was able to handle an I_d current of approximately $175A_{RMS}$ at a case temperature of approximately 114 °C. In the simulation, it was found to be able to flow at $150A_{RMS}$ at that temperature, but the margin was very small; therefore, if the device is affected by the outside temperature without forced cooling, it is very likely to fail, which can lead to a situation where large currents can flow in each phase and lead to thermal overheating, which can be dangerous. Even if an IMS board is used, a heat sink or forced cooling is necessary when considering a condition in which twice the rated current flows. Therefore, the following simulation shows the need for a cooling element, and it can be seen that the maximum temperature of the surface of the device in the inverter was definitely reduced when the module was operated with six modules, with the current flowing at two times the current rating of each module, and the maximum temperature of the device was maintained at 66.45 °C when the heat sink was attached and the air cooling was 1 m/s. When air is cooled, it is important to air cool in a direction that allows good heat transfer between the heat sink fins. It can be seen that the maximum surface temperature of the device was 35.3 °C lower in the simulation with air cooling in the parallel direction than in the cross direction. In addition, it can be observed that the temperature downstream of the heat sink was high, which means that the heated fluid in the heat sink dissipated well to the outside. In this simulation, the inverter was air-cooled; however, when used as an inverter mounted inside an outboard motor using water cooling, the inverter can be operated under better conditions.

After investigating the heat generation in the inverter under heavy current conditions, the CFD analysis of $60A_{RMS}$ and $80A_{RMS}$ continuous current corresponding to the capacity of the actual inverter is modeled as shown in Figures 9–11.

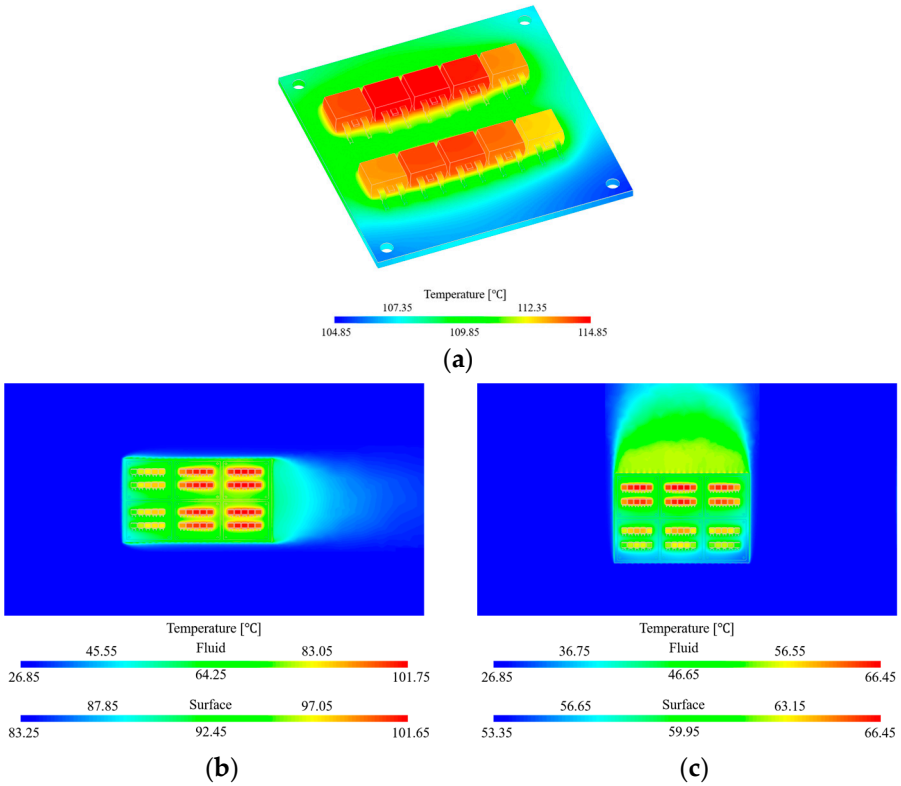

Figure 8. Thermal analysis of inverter at 2 times rated current conditions: (**a**) natural cooling condition; (**b**) forced cooling condition (cross); (**c**) forced cooling condition (parallel).

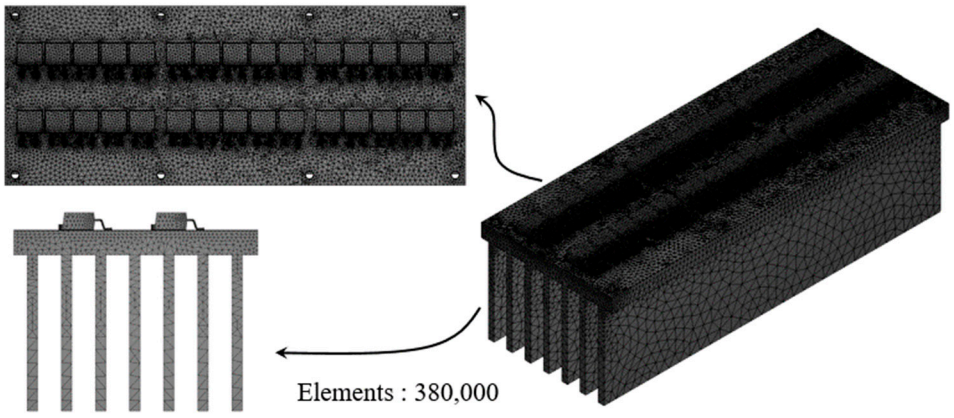

Figure 9. Thermal analysis model: 3 modules, natural cooling.

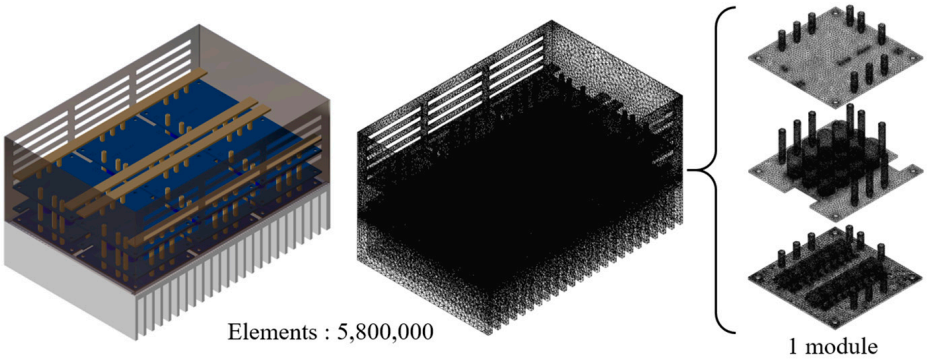

Figure 10. Thermal analysis model: 6 modules, natural cooling.

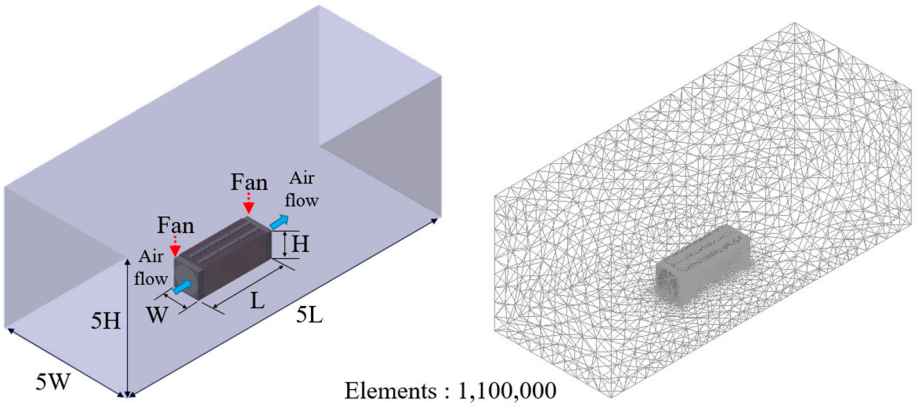

Figure 11. Thermal analysis model: 3 modules, forced cooling.

Figures 12 and 13 show the simulation results of the 80 A_{RMS} and 60 A_{RMS} design models in the natural cooling state. A heat sink with a fin length of 45 mm was used. In the upper part of Figure 10, the heat distribution of the device when an 80 A_{RMS} current was applied to the inverter, the heat was not concentrated, and the heat was evenly distributed throughout can be seen. The MOSFET device used in this inverter had a temperature saturation of 77.1 °C. Starting from about 100 °C on the reference, the higher the temperature, the less current the device was able to drive, which means that the point of degradation was around 100 °C, so we can interpret that there was a temperature margin of about 20 °C before this point. Figure 13 shows the analyzed results of the inverter under the condition that an equivalent current of 60A_{RMS} was flowing. The results showed temperature saturation at 63.9 °C. Without forced cooling, there was a margin of 36.1 °C, so we can see that the device was operating within the safe operating area (SOA) with natural cooing to 64% of the critical operating point of 100 °C. However, forced cooling was required to maintain a similar temperature level at the design point of the 80A_{RMS}, and the results are shown below.

Forced cooling is a form of cooling with an attached fan, so the flow field in the CFD simulation represents the movement of air in one direction. An image and results of the fluid motion in forced cooling are shown in Figures 14 and 15.

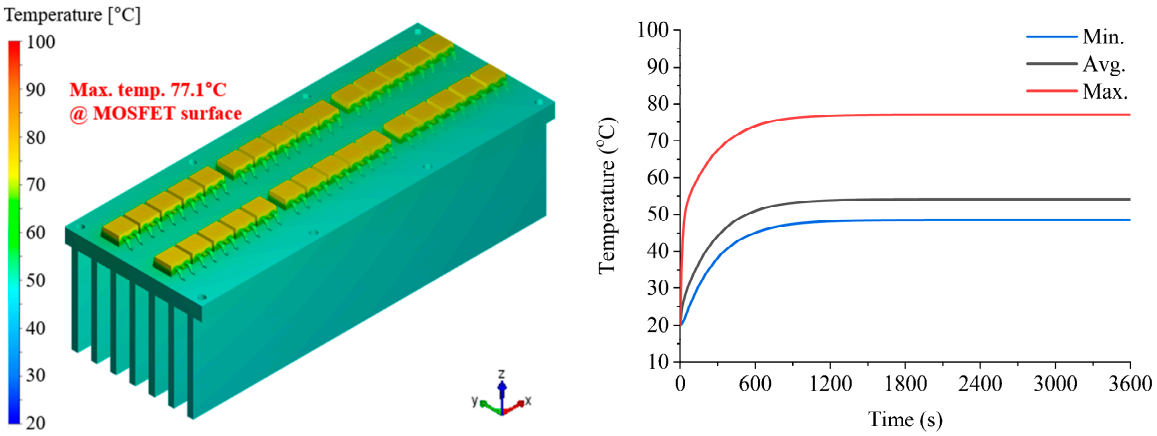

Figure 12. Thermal analysis simulation: 3 modules, 80A_{RMS}, natural cooling.

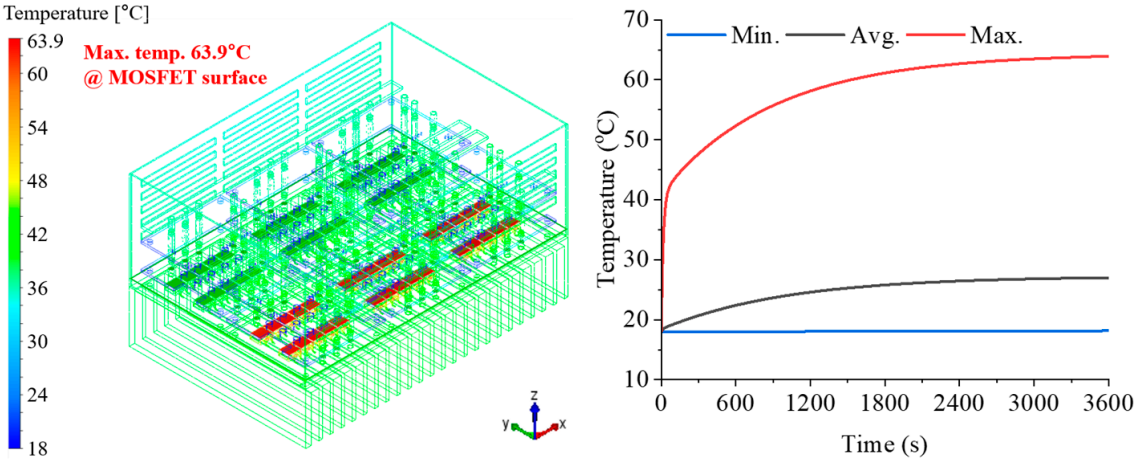

Figure 13. Thermal analysis simulation: 6 modules, $60A_{RMS}$, natural cooling.

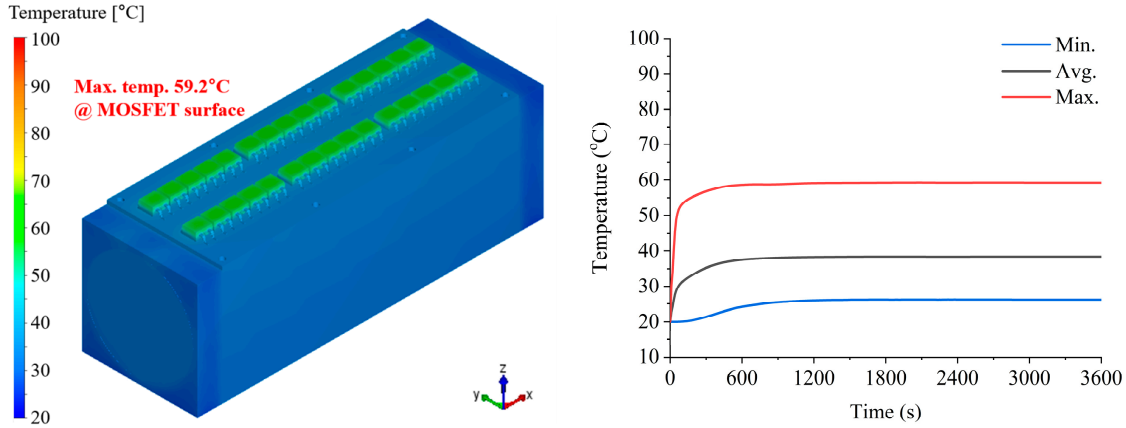

Figure 14. Thermal analysis simulation: 3 modules, $80A_{RMS}$, forced cooling.

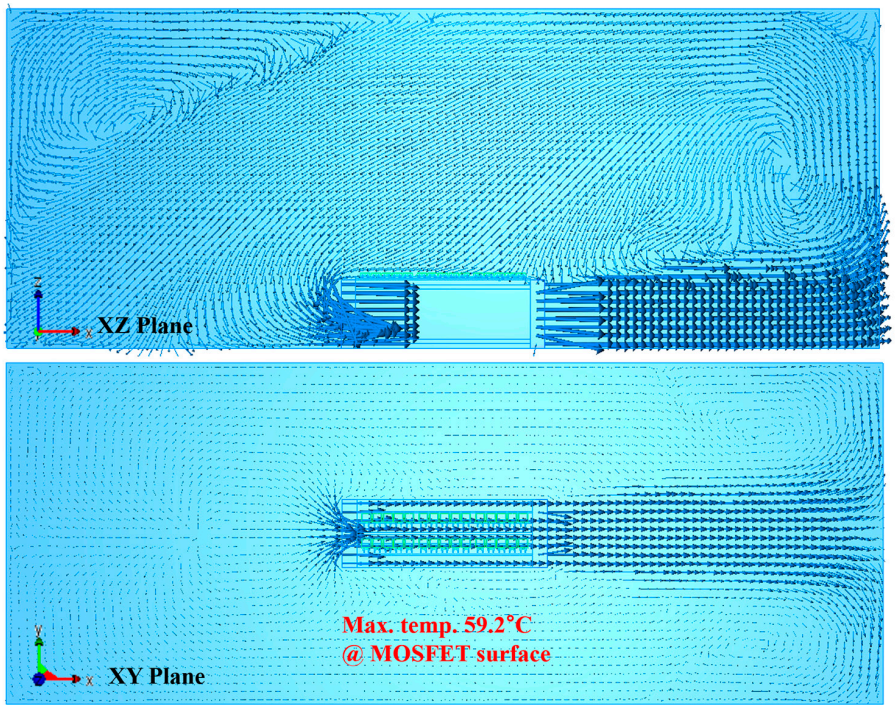

Figure 15. Thermal analysis simulation: flow diagram of air as a vector.

This forced cooling method is the result of attaching a heat sink with a fin length of 45 mm and forcing it to cool at a flow rate of 1 m/s. It can be seen that the temperature saturation point of the inverter reached 59.2 °C. In the case of natural cooling without forced cooling, the same $80A_{RMS}$ current value became saturated at 77.1 °C, showing a temperature reduction of 17.9 °C.

The temperature value of the MOSFET specified in the CFD simulation was based on the case temperature. The variables shown in Figure 16 are temperature and thermal resistance. The temperature of the inverter that was measured in the actual experiment was the temperature of the heat sink and the outer temperature of the MOSFET; therefore, the junction temperature needed to be obtained through Equation (6).

$$T_J - T_C = P \times \theta_{JC} \tag{6}$$

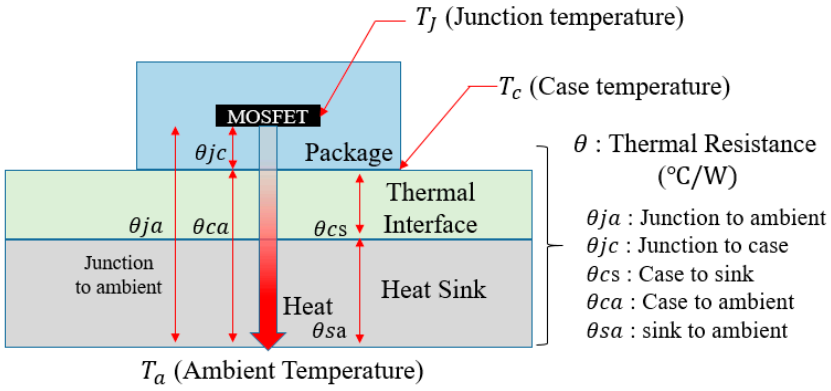

Figure 16. Relation between temperature and thermal resistance.

The parameter of θ_{JC} given in the MOSFET was 0.4 °C/W within T_C = 25 °C. The loss values per MOSFET were 0.864 W and 1.216 W at $60A_{rms}$ and $80A_{rms}$, so they were 0.3456 °C and 0.4864 °C, respectively. The temperature difference between the case and the junction was not very large and was within 1 °C, so the case temperature was sufficient to predict the failure tolerance temperature of the MOSFET.

3.2. Experimental Verification

An actual rated load test and a temperature saturation test of the surface-mounted permanent-magnet synchronous motors (SPMSMs) were performed to verify the comparison with the simulation. The load test device is shown in the figure above, and the temperature measurement was performed by directly attaching a thermocouple to the MOSFET case. The multi-phase inverter can be configured with one phase for each module, and six modules can be configured with six phases or dual three-phase configuration. Experimental verification was performed by driving a 3 kW three-phase motor with three modules and a 10 kW dual three-phase motor with six modules. The actual test configuration is show in Figure 17, and the load test of the test motor was performed using a load motor and a torque sensor. The actual multi-phase inverter configuration is shown in the lower right corner of Figure 17.

In Figure 18, we can see that the three-phase current remained around $60A_{RMS}$ for a 16 N·m load regardless of speed, and the inverter operated normally. To observe the temperature saturation, we set saturation as the standard when the temperature change was within 1 °C for 30 min; however, because the inverter was currently used for an outboard motor, we extracted the temperature trend graph at the rated load for approximately 60 min based on the battery used in the outboard. Therefore, it is not a perfect saturation result according to strict standards; however, when looking at the temperature trend graph in light of the actual operation of the outboard, it can be seen that the temperature trend graph was below approximately 45 °C. When looking at Figure 19, it can be seen that there was a difference of 18.9 °C compared to the maximum temperature of 63.9 °C in the simulation.

However, considering that the outdoor temperature in the actual test was 18 °C, it was 9 °C different from the simulation based on the outdoor temperature of 27 °C. There was a difference of 9.9 °C in the analysis results, and the corresponding value can be interpreted as a difference in the range of the HTC values of the air.

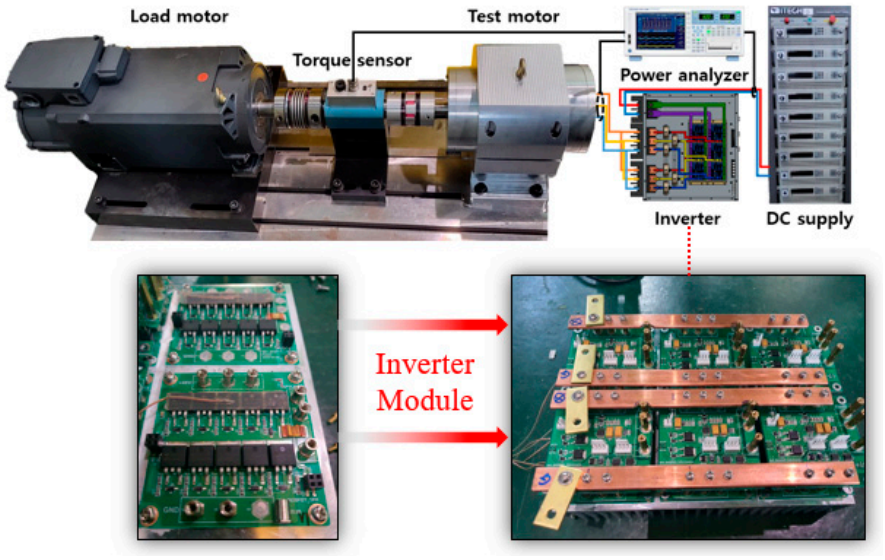

Figure 17. Inverter test setup with load motor.

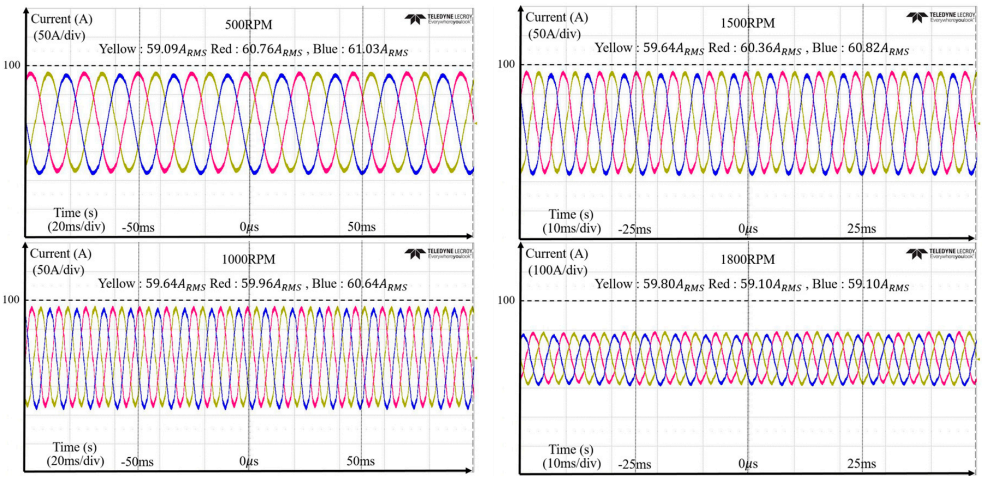

Figure 18. Phase current waveforms of the inverter at 16 N·m rated load torque.

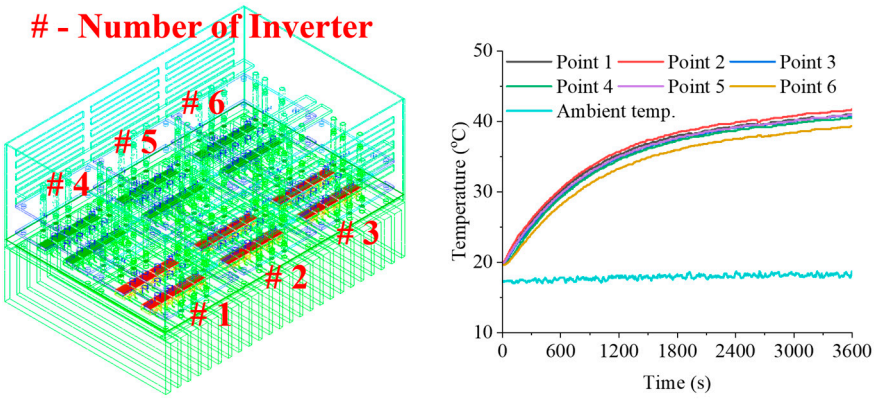

Figure 19. Thermal saturation test results at 16 N·m rated load torque.

In addition, variations within the motor and inverter and differences in the actual performance can also be considered as factors affecting the temperature difference. The performance map was obtained with a motor efficiency of 94% compared with the 92% considered in the actual design. It cannot be completely excluded that a 2% difference in the overall system and motor capacities could lead to higher current values than in the simulation. The performance map of the 3kW motor and inverter can be seen in Figure 20. A 10 kW motor was tested with the same inverter. As shown in Figure 21, a 10 kW motor was tested with the inverter configured in parallel for multi-phases. The parameters of the motor and the three-phase test structure are listed in Table 6. The simulation could be easily derived by utilizing the advantage of scalability with the reliability obtained from 3 kW module-by-module analysis; however, in the actual inverter test, the inverter configuration created by connecting each module was better than that of an independent inverter. However, it was vulnerable to noise problems; therefore, it was not easy to measure temperature. In the actual electric motor test, the inverter efficiency was 96% when the rated torque was 53 N·m; however, variables such as the back electromotive force, encoder angle, and inverter signal synchronization caused problems due to variables such as back-electromotive force, encoder angle, and inverter signal synchronization problems. In the inverter efficiency performance map, an efficiency of 98% was achieved in the low-torque region of the high-speed section. The efficiency and performance metrics associated with this 10 kW motor test are shown in Table 7 and Figure 22.

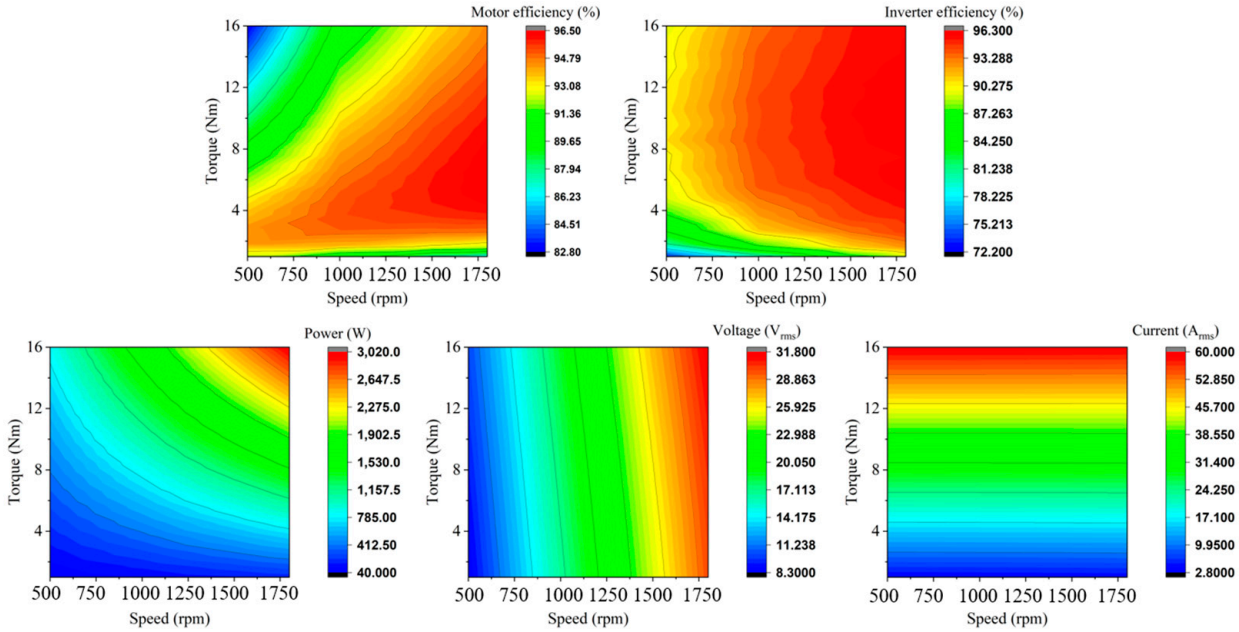

Figure 20. Performance map for a 3 kW motor.

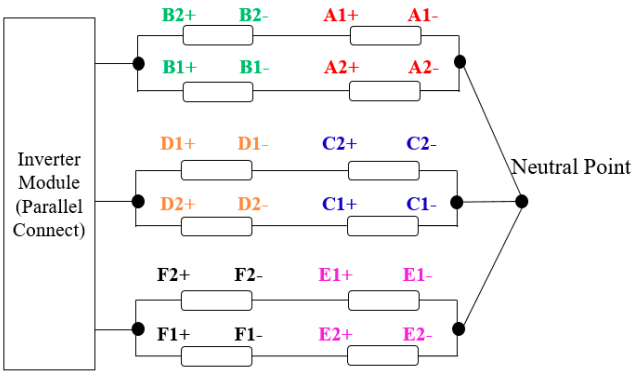

Figure 21. Wiring for dual 3-phase motor in multi-phase motor.

Table 6. Parameter values of 10 kW motor and inverter.

Parameters	Symbols	Values
Power	kW	10 kW
Rated speed	RPM	1800 RPM
Rated torque	N·m	53.05 N·m
Number of poles	-	10
Rated current	A_{RMS}	$200A_{RMS}$
Direct-axis inductance	H	36.66 μH
Quadrature-axis Inductance	H	36.05 μH
Quadrature-axis Flux linkage	Wb	25.19 mWb

Table 7. Test verification results of 10 kW multi-phase motor.

10 kW	U_1	U_2	U_3	I_1	I_2	I_3	P	Efficiency
1800 RPM	40.32	40.61	40.40	188.29	189.20	190.26	10.9k	96.746
	40.33	40.62	40.41	188.29	189.21	190.27	10.9k	96.743
	40.33	40.62	40.40	188.28	189.21	190.2	10.9k	96.763

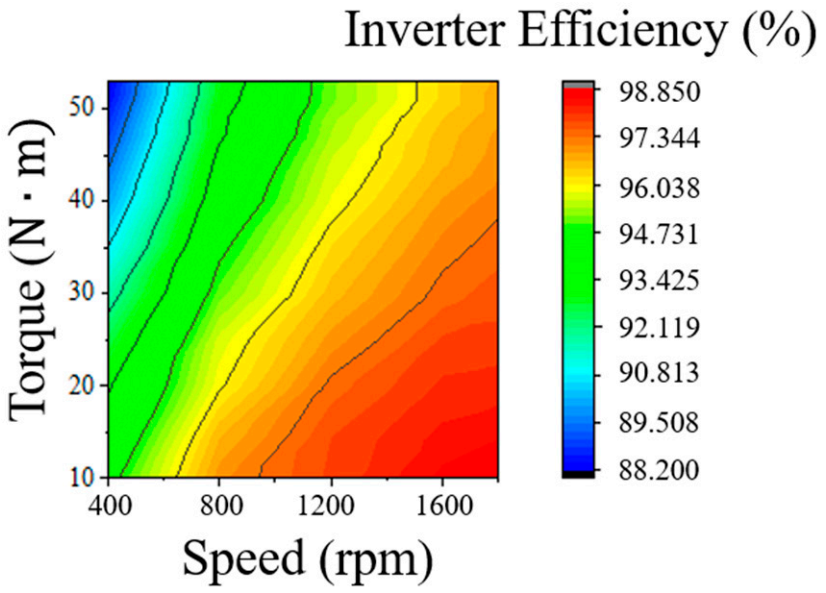

Figure 22. Performance map for a 10 kW inverter.

4. Conclusions

In this study, a modular inverter that can be used for multi-phase motors was designed using temperature analysis and power electronics simulations. Temperature analysis simulation and power electronics simulations were used to design a modular inverter that could be used for multi-phase motors and compared with experimental values. Owing to the need for an inverter that is easy to operate and allows us to change the capacity of an electric motor with a simultaneous three-phase structure and a multi-phase structure according to the wiring, a modular inverter was designed, and thermal analysis and power electronics analysis were performed for the stable operation of the inverter. However, it is not difficult to produce a stable inverter by performing only manual calculations and power electronics simulations. However, if a thermal analysis simulation is additionally performed, the loss expectation results that depend on the parameters of the power semiconductor devices and circuit analysis are more accurate than the other results. Variables

caused by the structure of the inverter and peripheral devices and variables related to temperature, such as external air temperature and heat diffusion, can be analyzed intuitively and are intuitively interpretable, with the added benefit of high visibility. Consequently, the operability and failure points of power semiconductor devices within the SOA of the inverter can be identified in detail. In addition, when comparing the module design and analysis results, it can be seen that the error between the simulation and actual test results was not as large as the difference in external temperature. As can be seen, if this process is always performed during inverter design, many errors in the actual test results can be reduced without overdesigning the inverter. Regardless of the specific application of the electric motor used in this study, it can always be applied to the design of inverters related to the electric motor, and it can be utilized to reduce design and development costs.

Author Contributions: Conceptualization, J.-W.K. and B.-G.P.; methodology, J.-W.K. and B.-G.P.; software, J.-S.P., T.-W.L. and J.-W.L.; validation, J.-S.P., T.-W.L., J.-W.L. and J.-W.K.; investigation, J.-S.P. and T.-W.L.; writing—original draft preparation, J.-S.P.; writing—review and editing, J.-S.P., B.-G.P. and J.-W.K.; supervision, J.-W.K.; project administration, J.-W.K.; funding acquisition, J.-W.K. All authors have read and agreed to the published version of the manuscript.

Funding: This research was supported by the Korea Electrotechnology Research Institute (KERI) primary research program through the National Research Council of Science and Technology (NST), which is funded by the Ministry of Science and ICT (MSIT, Republic of Korea) (No. 23A01082, "Development and Demonstration of a New Future Concept Electric Propulsion (KERI e-ship)").

Conflicts of Interest: The authors declare no conflict of interest.

References

1. Quere, C.; Andrew, R.; Friedlingstein, P.; Kaushik, R.; Sitch, S.; Hauck, J.; Pongratz, J.; Picker, P.; Ivar, K.; Peters, G.; et al. Global Carbon Budget 2018. *Earth Syst. Sci. Data* **2018**, *10*, 2147–2194. [CrossRef]
2. Tan, Y.; Nookuea, W.; Li, H.; Thorin, E.; Yan, J. Property impacts on Carbon Capture and Storage (CCS) processes: A review. *Energy Convers. Manag.* **2016**, *118*, 204–222. [CrossRef]
3. Barbara, B.; Maurizio, A.; Emilio, A.; Dario, B. Process analysis of a molten carbonate fuel cell on-board application to reduce vessel CO_2 emissions. *Chem. Eng. Process. Process Intensif.* **2023**, *190*, 109415.
4. Kaushik, R. Present Status and Future Trends in Electric Vehicle Propulsion Technologies. *J. Emerg. Sel. Top. Power Electron. IEEE* **2013**, *1*, 3–10.
5. Dinesh, K.; Firuz, Z. A Comprehensive Review of Maritime Microgrids: System Architectures, Energy Efficiency, Power Quality, and Regulations. *IEEE Access* **2019**, *7*, 67249–67277.
6. Husain, I.; Ozpineci, B.; Islam, M.S.; Gurpinar, E.; Su, G.J.; Yu, W.; Chowdhury, S.; Xue, L.; Rahman, D.; Sahu, R. Electric Drive Technology Trends, Challenges, and Opportunities for Future Electric Vehicles. *Proc. IEEE* **2021**, *109*, 1039–1059. [CrossRef]
7. Liu, Z.; Wu, J.; Hao, L. Coordinated and fault-tolerant control of tandem 15-phase induction motors in ship propulsion system. *IET Electr. Power Appl.* **2018**, *12*, 91–97. [CrossRef]
8. Sandro, C.; Daniel, F.; Roberto, P.; Mauro, B.; Mario, M.; Alberto, T. A Fully-Integrated Fault-Tolerant Multi-Phase Electric Drive for Outboard Sailing Boat Propulsion. In Proceedings of the 21st European Conference on Power Electronics and Applications, Genova, Italy, 3–5 September 2019.
9. Mohamed, A.F.; Julien, C.; Kritika, D.; Yassine, B.; Mohamed, E.B.; Omar, H. Multiphase Motors and Drive Systems for Electric Vehicle Powertrains: State of the Art Analysis and Future Trends. *Energies* **2023**, *16*, 768.
10. Matus, K.; Ludek, B.; Petr, B. Compensation methods of interturn short-circuit faults in dual three-phase PMSM. In Proceedings of the IECON 2020 The 46th annual Conference of the IEEE Industrial Electronics Society, Singapore, 18–21 October 2020; pp. 4833–4838.
11. Sun, W.; Liu, J.; Wei, S.; Gong, X. Heat dissipating structure design of an inverter with direct-cooling IGBT module for EV. In Proceedings of the IEEE Conference and Expo Transportation Electrification Asia-Pacific (ITEC Asia-Pacific), Beijing, China, 3 September–31 November 2014.
12. Aldo, K.; Andrea, C.; David, S.; Martin, S.; Markus, M.; Carlos, M. Evolution and Modern Approaches for Thermal Analysis of Electrical Machines. *IEEE Trans. Ind. Electron.* **2009**, *56*, 871–882.
13. Ye, J.; Yang, K.; Ye, H.; Emadi, A. A Fast Electro-Thermal Model of Traction Inverters for Electrified Vehicles. *IEEE Trans. Power Electron.* **2017**, *32*, 3920–3934. [CrossRef]
14. Dong, J.; Huang, Y.; Jin, L.; Lin, H.; Yang, H. Thermal Optimization of a High-Speed Permanent Magnet Motor. *IEEE Trans. Magn.* **2014**, *50*, 7018504. [CrossRef]
15. Ren, Y.; Xu, M.; Zhou, J.; Lee, F.C. Analytical loss model of Power MOSFET. *IEEE Trans. Power Electron.* **2006**, *21*, 310–319.

16. Shen, Z.J.; Xiong, Y.; Cheng, X.; Fu, Y.; Kumar, P. Power MOSFET Switching Loss Analysis: A New Insight. In Proceedings of the Conference Record of the 2006 IEEE Industry Applications Conference Forty-First IAS Annual Meeting, Tampa, FL, USA, 8–12 October 2006.
17. Utkarsh, J.; Faisal, M.; Hamid, A.M.; Peyush, P.; Mayank, C.; Sima, D. A Method for Selection of Power MOSFETs to Minimize Power Dissipation. *Electronics* **2021**, *10*, 2150.
18. Toni, L.; Reinhold, E. Current sharing of paralleled power MOSFETs at PWM operation. In Proceedings of the IEEE Power Electronics Specialists Conference 2016, Jeju, South Korea, 18–22 June 2006.
19. «POWERFORGE, Multi-Level by Design» Power Design Technologies SA. Available online: https://powerforge.powerdesign.tech (accessed on 30 September 2023).
20. «PLECS, The Simulation Platform for Power Electronic Systems» Plexim. Available online: https://www.powersimtech.com (accessed on 30 September 2023).
21. «Autodesk Simulation CFD». Available online: https://help.autodesk.com (accessed on 30 September 2023).
22. «Altair CFD». Available online: https://www.altair.com (accessed on 30 September 2023).
23. Singh, Y.; Bhattacharyya, S.K.; Idichandy, V.G. CFD approach to modelling, hydrodynamic analysis and motion characteristics of a laboratory underwater glider with experimental results. *J. Ocean Eng. Sci.* **2017**, *2*, 90–119. [CrossRef]
24. Mo, Q.; Guan, H.; He, S.; Liu, Y.; Guo, R. Guidelines for the computational domain size on an urban-scale VAWT. *J. Phys.* **2021**, *1820*, 012177. [CrossRef]
25. Jochen, F.; Christopher, M.; Wolfgang, R.; Lionel, T. Highly resolved large-eddy simulation of separated flow in a channel with streamwise periodic constriction. *J. Fluid Mech.* **2005**, *526*, 19–66.
26. Frank, P. *Incropera's Principles of Heat and Mass Transfer*; Global Ed.; Wiley: Hoboken, NJ, USA, 2017.
27. Buchmann, H.-F. *Properties and Applications of Epoxy Moulding Compounds*, 1st ed.; Duresco GmbH: Witterswil, Switzerland, 2019; pp. 1–13.
28. Lee, S.H.; Doe, J.K.; Song, H.H.; Kim, S.W.; Kang, K.H.; Lee, W.S. Thermophysical poperties of epoxy molding compound for microelectronic packaging. In Proceedings of the Seventeenth European Conference on Thermophysical Properties (ECTP), Bratislava, Slovak Republic, 5–8 September 2005.
29. Caplinq Blog. Available online: https://www.caplinq.com/blog/heat-capacity-of-epoxy-molding-compound_102/ (accessed on 25 September 2023).
30. Tang, H.; Li, W.; Li, J.; Gao, H.; Wu, Z.; Shen, X. Calculation and Analysis of the Electromagnetic Field and Temperature Field of the PMSM Based on Fault-Tolerant Control of Four-Leg Inverters. *IEEE Trans. Energy Convers.* **2020**, *35*, 2141–2151. [CrossRef]
31. Li, W.; Li, L.; Gao, H.; Li, D.; Zhang, X.; Fan, Y. Influence of direct-connected inverter with one power switch open circuit fault on electromagnetic field and temperature field of permanent magnet synchronous motor. *IET Electr. Power Appl.* **2018**, *12*, 815–825. [CrossRef]

Disclaimer/Publisher's Note: The statements, opinions and data contained in all publications are solely those of the individual author(s) and contributor(s) and not of MDPI and/or the editor(s). MDPI and/or the editor(s) disclaim responsibility for any injury to people or property resulting from any ideas, methods, instructions or products referred to in the content.